Journal of Applied Fluid Mechanics, Vol. 9, No. 3, pp. 1367-1379, 2016.
Available online at www.jafmonline.net, ISSN 1735-3572, EISSN 1735-3645.
DOI: 10.18869/acadpub.jafm.68.228.24322

Study of Heat Transfer over a Square Cylinder in Cross Flow using Variable Resolution Modeling

P. Ranjan and A. Dewan†

Department of Applied Mechanics, Indian Institute of Technology Delhi, Hauz Khas, New Delhi - 110016, India

†Corresponding Author Email: *dewan_anupam@yahoo.com*

(Received December 11, 2014; accepted April 29, 2015)

ABSTRACT

In the present study, a method of Partial-Averaged Navier-Stokes (PANS) equations, purported to perform variable resolution modeling, is used to predict the heat transfer over a square cylinder in a cross-flow. The PANS closure is based on the RANS SST k-ω model paradigm. The simulations were carried out using an open source software, namely, Open FOAM, at Reynolds number = 22000. The open source code and the PANS model are validated against the experimental work reported in the literature and it was observed that both the mean flow properties and turbulent statistics were in good agreement with the experimental results. Further the capability of the PANS approach in predicting heat transfer in turbulent flow is also studied. An algebraic wall function is used for the near wall treatment of the energy equation. The computed, average and local Nusselt numbers are compared with the experimental and LES results reported in the literature. The phase-averaged analysis of the shedding phenomenon is studied to understand the heat transfer phenomenon at different faces of the cylinder and turbulent heat fluxes are also considered to understand the effect of turbulence on convection.

Keywords: Turbulent heat transfer; Open FOAM; Partially-averaged navier-stokes (PANS); SST k-ω turbulence model.

1. INTRODUCTION

The need for an accurate prediction of turbulent heat transfer through a bluff body is encountered in many industrial applications, which include, composite materials that are less impervious to heat used in aeronautics industry, cooling towers, turbo-engines, cooling of electronic equipment and various heat exchange devices, etc. The complexity involved in these kinds of flow and heat transfer characteristics is due to separation of shear layers from the body and interaction of these shear layers in the near wake region formed by the separation behind the body. Therefore an accurate modeling technique is required to handle the complexity involved with a bluff body in a turbulent flow field. Thus the computational method which is to be used should be able to accurately capture the flow physics namely: recirculation, vortex shedding, wake region, and shear layer interaction, etc.

The most widely used models in industrial CFD tools for the aforementioned types of problems are those based on the RANS paradigm, which captures the mean flow properties but fails to predict turbulent scales. On the other hand, the LES approach is very promising for capturing flow fluctuations and turbulent scales. But, LES approach is computationally quite expensive when it comes to industrial applications because of complex geometries and large values of Reynolds number involved. Therefore a model is required which is computationally less expensive and also captures the turbulence phenomenon. Girimaji *et al.* (2006, a) and Girimaji (2006, b) proposed the Partially-Averaged Navier-Stokes equations (PANS) approach to meet the said requirements.

The PANS approach is a variable resolution method in which the extent of resolution is based on the turbulence kinetic energy distribution between eddies which are to be resolved and which are to be modeled. The details of the PANS approach can be found in Girimaji *et al.* (2006, a) and Girimaji (2006, b). Further Girimaji and Khaled (2005), Lakshmipathy and Girimaji (2006, 2007), Jeong and Girimaji (2010), Murthi *et al.* (2010), Basara *et al.* (2011), and Girimaji and Wallin (2013) have also provided the theoretical foundation. They have subsequently assessed the application of PANS approach to many isothermal flows associated with various geometries, such as, backward facing step, circular and square cylinders.

However, before PANS approach can be applied to practical problems concerned with heat transfer, it has to be tested with one of the benchmark

problems. Flow over a heated square cylinder, maintained at a constant temperature, is considered in the present paper to test the effectiveness of the PANS approach. The reason for choosing this flow configuration is, one, a large number of experimental studies have been reported in the literature to study its flow dynamics and, second, its similarity to typical flow over bluff body configuration encountered in many practical situations.

We first discuss experimental studies reported in the literature that are relevant to flow past a square cylinder. Durao *et al.* (1988) used laser-Doppler velocimetry (LDV) to measure the turbulent flow properties of a square cylinder with Reynolds number based on the cylinder height of 1.4×10^4. They performed experiments in a water channel with blockage ratio of 0.14. Similarly Lyn and Rodi (1994) and Lyn *et al.* (1995) also performed experiments with LDV at Reynolds number of 2.2×10^4. The former focused their studies on shear-layer and recirculation regions and the later focused on near wake flow around the cylinder. Only few experimental studies have been reported in the literature on heat transfer from a square cylinder in cross flow. Igarshi (1985), Ahmed and Yovanovic (1997) and Yoo *et al.* (2003) provided the mean values of the Nusselt number and derived empirical correlation for the global Nusselt number with respect to Reynolds number.

Further a large number of studies concerning computational analysis of flow field calculations for a square cylinder using various modeling methodologies have been reported in the literature, but to the best of author's knowledge, only a couple of studies have been reported concerning forced convective heat transfer in a flow past a heated square cylinder. Both Wiesche (2007) and Boileau *et al*. (2013) used LES approach to predict heat transfer around a square cylinder. Boileau *et al.* (2013) showed the effectiveness of LES with unstructured grid. However, as already stated, LES is still very expensive in terms of the computational resources required and is not feasible for industries to afford such computational demand.

In the present work, flow dynamics and heat transfer from a square cylinder kept in cross flow are investigated using the PANS approach, which is a variable resolution model, capable of predicting scales of turbulence depending on the need. Therefore unsteady flow past a heated square cylinder, with diameter *d*, at fixed surface temperature (T_w) is investigated at a Reynolds number of $Re_d = 2.2\times10^4$ for an incompressible fluid with *Pr = 0.7* (air). The results obtained are compared with the experimental data of Lyn and Rodi (1994) and Lyn *et al.* (1995) and with the LES predictions of Boileau *et al.* (2013). Therefore the current study presents the capability of PANS approach to provide insight into the heat transfer in the wake region of a bluff body.

The paper is organized as follows. In section 2 the equations governing the fluid flow and heat transfer are presented along with the detailed formulation of the PANS approach used in the present work. Section 3 provides the details about the geometry, physical conditions and numerical schemes used in the present study. Finally section 4 presents all results and their comparison with the experimental data. At last the unsteady flow field with heat transfer over a square cylinder is investigated and credibility of PANS approach is concluded.

2. GOVERNING EQUATIONS

2.1 Basis of PANS Approach

In this section, the Partially-Averaged Navier-Stokes (PANS) equations are briefly summarized as given by Girimaji *et al.* (2006, a) and Girimaji (2006, b). Starting from the instantaneous incompressible flow equations

$$\frac{\partial V_i}{\partial t}+V_j\frac{\partial V_i}{\partial x_j}=-\frac{\partial p}{\partial x_i}+\nu\frac{\partial^2 V_i}{\partial x_j\partial x_j} \tag{1}$$

$$\frac{\partial V_i}{\partial x_i}=0 \tag{2}$$

We define $\langle\ \rangle$ as an arbitrary filter which commutes with both spatial and temporal differentiations. Thus by applying this filter to the instantaneous velocity field it can be decomposed as

$$V_i = U_i + u_i \tag{3}$$

where $U_i=\langle V_i\rangle$ is the filtered/resolved field, u_i the residual/fluctuation field that needs to be modeled. Each of the filtered velocity field satisfies the continuity equations separately, such that

$$\frac{\partial U_i}{\partial x_i}=\frac{\partial u_i}{\partial x_i}=0 \tag{4}$$

It is well understood that for this type of arbitrary filtering process, the average of the unresolved velocity and the correlation between resolved and unresolved velocities are non-zero, i.e., $\langle u_i\rangle\neq0, \langle U_i u_i\rangle\neq0$.

Now applying this arbitrary filter to the equation of motion we get

$$\frac{\partial U_i}{\partial t}+U_j\frac{\partial U_i}{\partial x_j}=-\frac{\partial\langle p\rangle}{\partial x_i}+\nu\frac{\partial^2 U_i}{\partial x_j\partial x_j}-\frac{\partial\tau\left(V_iV_j\right)}{\partial x_j} \tag{5}$$

$$\nabla^2\langle p\rangle=-\frac{\partial U_i}{\partial x_j}\frac{\partial U_i}{\partial x_j}+\frac{\partial^2\tau\left(V_iV_j\right)}{\partial x_j\partial x_j} \tag{6}$$

In equations (5) and (6), $\tau\ (V_iV_j)$ denotes the generalized central second moment tensor and is defined as the sub-filtered shear (SFS) stress. It is given by the expression

$$\begin{aligned}\tau(f,g)&=\langle fg\rangle-\langle f\rangle\langle g\rangle\\ \tau(f,g,h)&=\langle fgh\rangle-\langle f\rangle\tau(g,h)-\langle g\rangle\tau(h,f)\\ &\quad-\langle h\rangle\tau(f,g)-\langle f\rangle\langle g\rangle\langle h\rangle\end{aligned} \tag{7}$$

Based on equation (7) the sub-filter kinetic energy and dissipation are given as

$$k_u = \frac{1}{2}\tau\left(V_i V_j\right); \varepsilon_u = \nu\tau\left(\frac{\partial V_i}{\partial x_j}\frac{\partial V_i}{\partial x_j}\right) \tag{8}$$

All properties with the subscript u indicate the PANS statistics. The RANS kinetic energy and dissipation are represented by k and ε, respectively. Equations (7) and (8) reduce to their RANS counterpart, when averaging is performed over all the scales of motion (denoted by an over bar). Further according to Germano (1992) the RANS statistics are related to its PANS counterpart as

$$\begin{aligned} &\overline{V_j} = \overline{\langle V_j \rangle} = \overline{U_j}; \\ &R\left(V_i V_j\right) \equiv \overline{V_i V_j} - \overline{V_i}\,\overline{V_j} = \overline{\tau\left(V_i V_j\right)} + R\left(U_i U_j\right) \end{aligned} \tag{9}$$

It can be observed from the above set of equations (1) to (9) that the governing equations obtained after filtering are invariant to the filter used and consequently the modeling of SFS stress term must be invariant to the type of averaging. Hence to model the SFS term any modeling approach based on the RANS paradigm can be used.

The arbitrary filter used in equation (3) was defined by Girimaji *et al.* (2006, a) and Girimaji (2006, b) in terms of the fraction of kinetic energy and dissipation associated with the scales to be modeled rather than on basis of the cut-off wave number, as in LES. They quantified it as the ratios of the unresolved to total kinetic energy and dissipation and it is given by

$$f_k = \frac{k_u}{k}; f_\varepsilon = \frac{\varepsilon_u}{\varepsilon} \tag{10}$$

Where f_k and f_ε are termed as the resolution control parameters. It is well known that much of the kinetic energy is contained in large scales and most of the dissipation occurs in the smallest scales due to which $0 \le f_k \le f_\varepsilon \le 1$. Further they showed that, mathematically, when f_k tends to zero, the model approaches DNS behavior as it resolves more scales of motion.

2.2 RANS *k-ω* Type SFS Stress Closure

For the SFS shear stress the Boussinesq assumption is invoked in combination with the averaging-invariance property for arbitrary filters,

$$\tau\left(V_i V_i\right) = \nu_u\left(\frac{\partial U_i}{\partial x_j} + \frac{\partial U_j}{\partial x_i}\right) - \frac{2}{3}k_u\delta_{ij} \tag{11}$$

where, $\nu_u = C_\mu \frac{k_u^{\,2}}{\varepsilon_u}$ and it denotes the unresolved eddy viscosity. Therefore to obtain a closure for the SFS stress term, k_u and ε_u have to be given or modeled. This can be achieved by using any of the previously proposed models of RANS paradigm. In the present work the SST *k-ω* model, given by Menter (1993, 1994), is used to close the set of equations (5) to (11). According to Menter (1994) equations for k and ω are

$$\frac{\partial(\rho k)}{\rho t} + \frac{\partial\left(\rho U_j k\right)}{\partial x_j} = \widetilde{P_k} - \beta^*\rho\omega k + \frac{\partial}{\partial x_j}\left(\Gamma_k \frac{\partial k}{\partial x_j}\right) \tag{12}$$

$$\begin{aligned} \frac{\partial(\rho\omega)}{\partial t} + \frac{\partial\left(\rho U_j \omega\right)}{\partial x_j} &= \frac{\gamma}{\nu_t}P_k - \beta\rho\omega^2 + \frac{\partial}{\partial x_j}\left(\Gamma_\omega \frac{\partial\omega}{\partial x_j}\right) \\ &+ \left(1 - F_1\right)2\rho\sigma_{\omega 2}\frac{1}{\omega}\frac{\partial k}{\partial x_j}\frac{\partial k}{\partial x_j} \end{aligned} \tag{13}$$

$$\text{With, } \nu_t = \frac{a_1 k}{\max\left(a_1\omega, \sqrt{2}S_2 F_2\right)} \tag{14}$$

To derive the PANS SST *k-ω* model from the above closure, steps given by Girimaji *et al.* (2006, a) and Girimaji (2006, b) are followed and the final equations are

$$\omega_u = \frac{\varepsilon_u}{\beta^* k_u}, f_\omega = \frac{\omega_u}{\omega} = \frac{\varepsilon_u \big/ \beta^* k_u}{\varepsilon \big/ \beta^* k} = \frac{f_\varepsilon}{f_k} \tag{15}$$

$$\begin{aligned} \frac{\partial(\rho k_u)}{\rho t} + \frac{\partial\left(\rho U_j k_u\right)}{\partial x_j} &= \widetilde{P_{ku}} - \beta^*\rho\omega_u k_u \\ &+ \frac{\partial}{\partial x_j}\left(\Gamma_{ku}\frac{\partial k_u}{\partial x_j}\right) \end{aligned} \tag{16}$$

$$\begin{aligned} \frac{\partial(\rho\omega_u)}{\partial t} + \frac{\partial\left(\rho U_j \omega_u\right)}{\partial x_j} &= \frac{\gamma}{\nu_u}P_{ku} \\ &- \left(\frac{1}{f_\omega} - 1\right)\frac{\gamma\beta^*}{\nu_u}\omega_u k - \frac{\beta\rho\omega_u^2}{f_\omega} \\ &+ \frac{\partial}{\partial x_j}\left(\Gamma_{\omega u}\frac{\partial\omega_u}{\partial x_j}\right) \\ &+ \left(1 - F_{1u}\right)2\rho\sigma_{\omega 2}\frac{f_\omega}{f_k}\frac{1}{\omega_u}\frac{\partial k_u}{\partial x_j}\frac{\partial k_u}{\partial x_j} \end{aligned} \tag{17}$$

$$\begin{aligned} &\Gamma_{ku} = \mu + \frac{\mu_u}{\sigma_k}\frac{f_\omega}{f_k}, \Gamma_{\omega u} = \mu + \frac{\mu_u}{\sigma_\omega}\frac{f_\omega}{f_k}, \\ &P_{ku} = \tau_{xy}\frac{\partial U_i}{\partial x_j}, \widetilde{P_{ku}} = \min\left(P_{ku}; c_l\varepsilon_u\right) \end{aligned} \tag{18}$$

$$\begin{aligned} &F_{1u} = \tanh\left(\arg_1^4\right), \\ &\arg_1 = \min\left(\max\left(\frac{\sqrt{k_u}}{\beta^*\omega_u y}; \frac{500\nu}{y^2\omega_u}\right); \frac{4\rho\sigma_{\omega 2}k_u}{CD_{k\omega u}y^2}\right) \end{aligned} \tag{19}$$

$$CD_{k_u\omega_u} = \max\left(2\rho\sigma_{\omega 2}\frac{1}{\omega_u}\frac{\partial k_u}{\partial x_j}\frac{\partial\omega_u}{\partial x_j}; 1.0e^{-10}\right) \tag{20}$$

$$F_{2u} = \tanh\left(\arg_2^2\right),$$
$$\arg_2 = \max\left(2\frac{\sqrt{k_u}}{\beta^* \omega_u y}; \frac{500\nu}{y^2 \omega_u}\right) \quad (21)$$

With $\mu_u = \frac{f_k}{f_\omega}\mu_t$ and the values of the model coefficients are the same as those used by Menter (1994): $\sigma_{k1} = 2$, $\sigma_{\omega 1} = 2$, $\beta_1 = 0.075$, $\beta^* = 0.09$, $c_1 = 10$, $\sigma_{k2} = 1$, $\sigma_{\omega 2} = 1.168$, $\gamma_2 = 0.4403$, $\beta_2 = 0.0828$, $\kappa = 0.41$.

Near the wall, automatic wall treatment given by Menter and Esch (2001) is used, which is insensitive to wall grid density and takes advantage of the fact that analytical solutions for both the sub layer and the logarithmic region are known:

$$\omega_{vis} = \frac{6\nu}{0.075 y^2}; \quad \omega_{\log} = \frac{1}{0.3\kappa}\frac{u_\tau}{y} \quad (22)$$

and can be reformulated in terms of y^+ and a smooth blending as

$$\omega_p\left(y^+\right) = \left[\omega_{vis}^2\left(y^+\right) + \omega_{\log}^2\left(y^+\right)\right]^{0.5} \quad (23)$$

Similarly velocity profile near the wall is given as:

$$u_\tau^{vis} = \frac{U}{y^+}; u_\tau^{\log} = \frac{U}{\frac{1}{\kappa}\ln\left(y^+\right) + 5};$$
$$u_\tau = \left[\left(u_\tau^{vis}\right)^4 + \left(u_\tau^{\log}\right)^4\right]^{0.25} \quad (24)$$

For k equation a zero flux boundary condition is applied.

Analogous to the modeling of the SFS stress, the turbulent heat flux vector is also modeled with the help of the turbulent diffusivity:

$$\left\langle u_i T' \right\rangle = -\alpha_t \frac{\partial T}{\partial x_i} = -\frac{\nu_u}{\mathrm{Pr}_t}\frac{\partial T}{\partial x_i}, \quad \text{with} \quad \mathrm{Pr}_t = \frac{\nu_u}{\alpha_t} \quad (25)$$

where, α_t and Pr_t are turbulent diffusivity and turbulent Prandtl number, respectively.

Therefore with no source terms and constant property assumptions the temperature equation can be written as

$$\frac{\partial \rho T}{\partial t} + \frac{\partial \rho U_j T}{\partial x_j} = \frac{\partial}{\partial x_j}\left[\left(\frac{\mu}{\mathrm{Pr}} + \frac{\mu_u}{\mathrm{Pr}_t}\right)\frac{\partial T}{\partial x_j}\right] \quad (26)$$

In Equation (26) Pr is the fluid property and the turbulent Prandtl number, Pr_t is set to a constant value of 0.9 (Boileau *et al.,* 2013).

For the treatment of the temperature equation near the wall, an algebraic formulation given by Kader (1981) is used here:

$$\Theta^+ = Pr.y^+ e^{-\Gamma} + \left[2.12\ln\left(1 + y^+\right) + \beta(\mathrm{Pr})\right]e^{-\Gamma}$$
$$\beta(\mathrm{Pr}) = \left(3.85\mathrm{Pr}^{1/3} - 1.3\right)^2 + 2.12\ln(\mathrm{Pr}) \quad (27)$$

with $\Gamma = \frac{0.001\left(Pr.y^+\right)^4}{1 + 5Pr.y^+}$ and $\Theta^+ = \frac{T_w - T}{T_\tau}$;

$T_\tau = \frac{q_w}{\rho c_p u_\tau}$ where u_τ is the friction velocity.

3 FLOW CONFIGURATION

3.1 Geometry and Physical Conditions

The computational domain used in the present case is shown in Figure 1. All dimensions are considered as a function of the cylinder's side length d =10 mm. The grid (Figure 2) used in the current study is based on that used by Jeong and Girimaji (2010), Barone and Roy (2006) and Lubcke *et al.* (2001) and these details are summarized in Table 1.

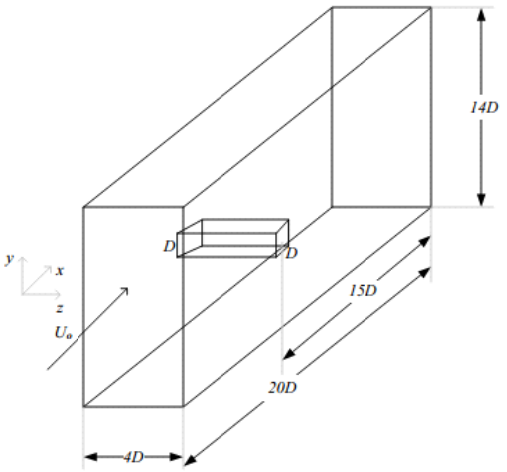

Fig. 1. Computational domain used in present study.

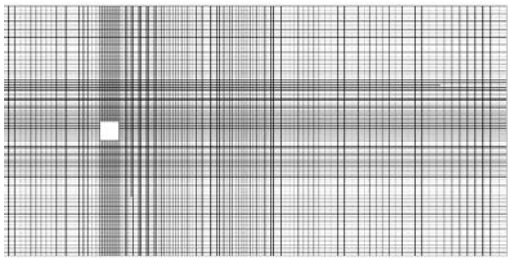

Fig. 2. Side view of computational grid.

The following boundary conditions are prescribed:

1. The no-slip condition for the velocity and a fixed temperature (T_w) on the square cylinder all along the spanwise direction are applied.
2. The periodic conditions are prescribed on the lateral sides, so as to compensate for the large

Table 1 Meshing strategies used in various studies

	Type	N_{xy}	N_z	N
Barone and Roy (2006), DES simulation	Coarse	9800	32	313,600
	Medium	39200	64	2,508,000
	Fine	88200	96	8,467,200
Lubcke *et al.* (2001)	LES,	32304	32	1,033,728
	RANS (2D)	8750 (125×70)	NA	8750
Jeong and Girimaji (2010)	PANS-STD k-ε	10165 (95×107)	27	274,455
Present	PANS	15000 (150×100)	32	480,000

span length used in the experiment of Lyn and Rodi (1994).

3. At the inlet, a uniform flow ($u_x = U_\infty$, $u_y = u_z = 0$) based on $Re = 2.2\times10^4$ and a uniform inflow temperature (T_{amb}) are prescribed. At the outlet atmospheric pressure condition is applied.
4. For the top and bottom planes, a slip condition is applied, considering a thin boundary on the wind tunnel walls of the experiment and are maintained at free stream temperature.

3.2 Numerical Treatment

Simulations were performed using a finite-volume based open source code Open FOAM. The existing SST k-ω model code was modified according to the PANS equations. The spatial discretization was carried out using the standard Gaussian finite volume integration method with different interpolation schemes. For the gradient terms a linear interpolation of the second order accuracy was implemented. The second order linear interpolation scheme was used for the Laplacian terms while second order upwind scheme was used for the divergence terms. The temporal discretization was performed using the second order implicit method. The PIMPLE algorithm of Open FOAM, a combination of PISO and SIMPLE algorithms, was used to couple the momentum and pressure equations. This algorithm rectifies the second pressure correction and then corrects both pressure and velocity explicitly (Jasak, 1996). The pre-conditioner conjugate gradient (PCG) iterative method with a diagonal based incomplete Cholesky (DIC) was used to solve the pressure equation. For all other equations the preconditioned bi-conjugate gradient (PBiCG) solver with the diagonal incomplete LU (DILU) decomposition pre-conditioner was applied.

3.3 Averaging Procedure

The data obtained was averaged in the spanwise direction, considering it to be statistically homogeneous, by taking values at eight different locations in the z-direction. Two types of averaging were performed as suggested by the experimental procedure of Lyn and Rodi (1994):

1. Time-averaging was done for $400D/U_0$ seconds (approximately 40 periodic cycles) once the flow reached the statistically stationary state (after approximately 400 cycles).
2. Phase averaging was done by averaging any flow property over a constant phase angle for every vortex shedding cycle. As given by Lyn and Rodi (1994), φ is obtained from a pressure signal p(t), measured by the spanwise averaging at center of the top face of cylinder, as shown in Figure 3a. The filtering of the instantaneous pressure signal $p(t)$ was done through a low pass second-order Butterworth filter with cut-off frequency equal to the shedding frequency, as shown in Figure 3a. Time was non-dimensionalized as $t^+ = t/t_c$, where t_c is the flow time. A pair of each peak and valley is defined as the half of the vortex shedding cycle. The shedding frequency was obtained by the fast Fourier transform of instantaneous pressure signal as shown in Figure 3b. The reference phase angle ($\varphi = 0$) was taken in accordance with the heat transfer study of Boileau *et al.* (2013) as shown in Figure 3a. For the flow properties, as the results are compared with those of Lyn *et al.* (1995), $\varphi = 0$ was taken at one of the peak of the periodic signal.

4 RESULTS AND DISCUSSIONS

Firstly the flow dynamics characteristics of flow over square cylinder are compared with the experimental results reported in the literature to evaluate the accuracy of the open source code and the PANS strategy used. Further onwards in all the results, velocity normalization is done by U_∞ (free stream velocity) and length is normalized by d (cylinder diameter), unless specified otherwise. The sections at which various results are plotted are shown in Figure4.

Initially a 2D steady RANS simulation using the SST k-ω model was carried out to determine the values of parameters k and ω. Using the values of k and ω, the Taylor scale of turbulence $\left(\Lambda = k^{1.5}/\varepsilon\right)$ was calculated, which was further used to determine the value of f_k based on the expression given by the Girimaji and Khaled (2005)

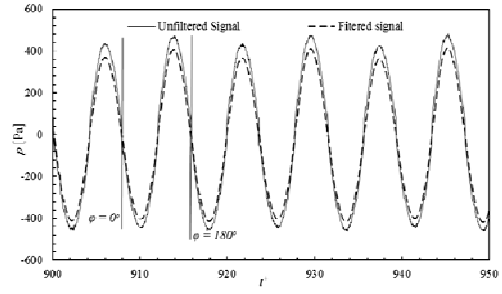

(a)

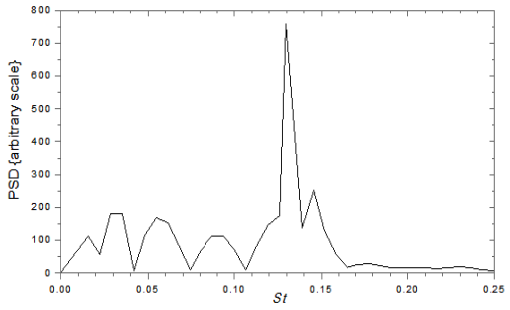

(b)

Fig. 3. (a) Unfiltered and low pass filtered pressure signal and (b) FFT of unfiltered pressure signal.

$$f_k\left(x\right)=\frac{1}{\sqrt{C_\mu}}\left(\frac{\Delta}{\Lambda}\right)^{\frac{2}{3}}\approx 3\left(\frac{\Delta}{\Lambda}\right)^{\frac{2}{3}} \tag{28}$$

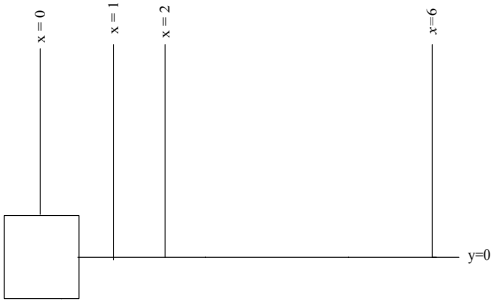

Fig. 4. Various sections at which results are considered.Validation of the Flow Dynamics.

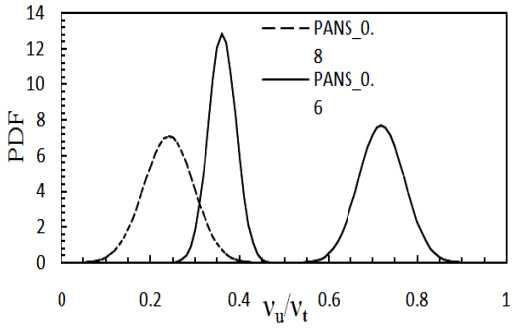

Fig. 5. PDF of viscosity recovery.

where $\varepsilon=\omega\times\beta^{*}k$ and $\Delta=\left(\left(\Delta_x\times\Delta_y\right)^{\frac{1}{2}}\right)$ is the grid size. Based on this a *priori* calculation the value of f_k comes out to be 0.6, and f_ε is taken as unity considering all the dissipation occurs at the smallest scales of motion which are to be modeled. But a *posteriori* validation is necessary to check whether the considered value of f_k will be able to produce the necessary physical system based on the imposed theoretical filter. As suggested by Lakshmipathy and Girimaji (2007) the recovery of turbulent viscosity ratio by PANS from the parent RANS model is a good parameter to check the amount of physical filtration achieved. We know that for RANS modeling $\nu_t=C_\mu\frac{k^2}{\varepsilon}$ and similarly for PANS approach $\nu_u=C_\mu\frac{k_u^{\,2}}{\varepsilon_u}$. Therefore the viscosity recovery is given by the expression $\frac{\nu_u}{\nu_t}=\frac{f_k^2}{f_\varepsilon}=f_k^2$, if f_ε is considered to be unity. Thus to conduct this *posteriori* validation, three values of f_k (0.8, 0.6 and 0.4) were considered for the PANS simulations. The probability density function (PDF) of the viscosity recovery ratio were then calculated for all three PANS simulations based on the 2D RANS simulation carried out initially. Figure 5 shows the PDF plots of the viscosity ratio for different f_k values. It can be observed that for f_k = 0.6 the plot shows peak nearly at 0.37 which is quiet close to f_k^2. For f_k = 0.8 and 0.4 the peaks achieved are at approximately 0.72 and 0.24 respectively. These values do not correspond to the desired value of the viscosity recovery (f_k^2). From this discussion it can be said that for the present grid system the value of f_k = 0.6 is able to achieve the required physical behavior for the flow field concerned.

Now the validation of the flow behavior is to be done to test the current modeling strategy and the open source code used to carry out the simulations. The first major check for any computational study on bluff bodies is an assessment of the integral properties, such as, Strouhal number (*St*), mean drag coefficient (C_D), and root-mean-square (r.m.s.) lift coefficient (C_L). Many experimental studies are available for the similar *Re* range and these are tabulated in Table 2. It can be observed from Table 2 that the values of *St* for square cylinder in a cross flow at *Re* = 22000 ranges from 0.12 to 0.138. Figure 3a shows a recorded pressure signal. Subsequently a Fourier-transform of this instantaneous pressure signal is performed and the frequency is normalized by D/U_∞ according to the definition of *St*. Figure 3b shows the spectra of *St,* which shows that there is only one dominant peak which corresponds to the value of 0.129. This value is well within the range of that observed experimentally. Similarly the values of $(C_D)_{mean}$ and $(C_L)_{rms}$ are also in the same range as given by the Lyn *et al.* (1995) and LES predictions of Boileau *et al.* (2013).

Further the present results of the flow dynamics quantities are also compared with the experimental data of Lyn *et al.* (1995). In Figure 6, the streamwise variation of the time-averaged and

Table 2 Global integrated flow parameters.

Case	Re	St	$(C_D)_{mean}$	$(C_L)_{rms}$	l_r^c
Durao *et al.* (1988), EXP	22000	0.133	-	-	1.33
Lyn *et al.* (1995), EXP	14000	0.126-0.132	2.1	-	1.38
Boileau *et al.* (2013), LES	22000	0.13	2.11	1.37	1.25
Wiesche (2007), LES	22000	0.19	-	-	1.15
Present, PANS	22000	0.129	1.98	1.35	1.31

fluctuating velocities are plotted at the center-line (y = 0). The experimental results of Lyn *et al.* (1995), Durao *et al.* (1988) and LES results of Boileau *et al.* (2013) are also included in Figure 6 for comparisons. From Figure 6a, a strong variation in the mean flow field is observed near the cylinder base region, which is mainly because of strong interaction between the separated shear layers from the top and bottom walls of the cylinder. In the near wake region further downstream (x > 3), the variation in the mean flow is quite small. Similar to LES results the current model also over predicts the velocity for most of the downstream regions, showing faster recovery of the streamwise velocity after the separation. At regions close to the cylinder (x = 2), as the streamwise velocity is overpredicted, a shorter recirculation length compared to the experimental values is observed (Table 2).

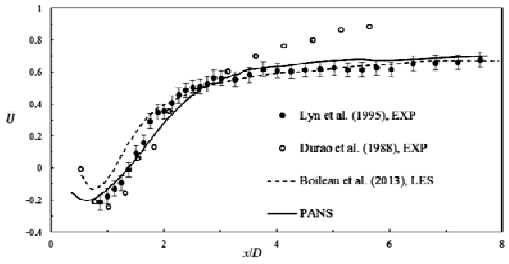

(a)

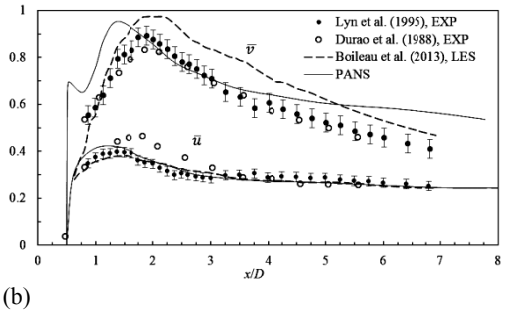

(b)

Fig. 6. Profiles of (a) time–averaged mean streamwise and (b) time averaged fluctuating velocity at centerline (y = 0).

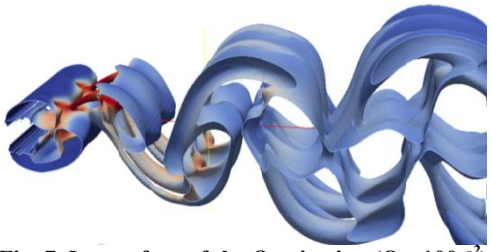

Fig. 7. Iso-surface of the Q-criterion (Q=-100s^{-2}) colored by dynamic viscosity ratio.

It can be observed from Figure 6a that in the present results and those by Lyn *et al.* (1995), the recovery of the mean velocity at the centerline is slow as compared to that observed by Durao *et al.* (1988). This deviation can be attributed to a larger wake region formed in the present case at high *Re* (22000) than that observed by Durao *et al.* (1988) in their experiments conducted at *Re* = 14000.

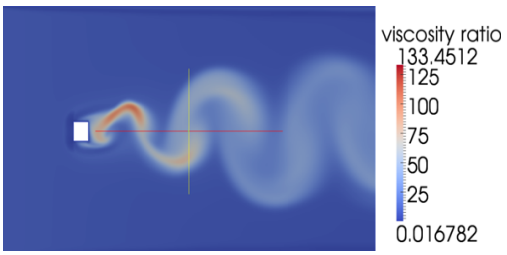

Fig. 8. Dynamic viscosity ratio distribution.

Figure 6b shows a variation of the time-averaged velocity fluctuations in the streamwise and transverse directions at the centerline. It can be seen that both streamwise and transverse velocity fluctuations are very well within the experimental range of Lyn *et al.* (1995). Figure 6b shows higher values of $\overline{v}$ than those of $\overline{u}$ in the wake region, at all x values, with a maximum value of approximately 0.9, which is due to the strong recirculation in the separation region. The current PANS results show that the transverse fluctuations match with the experimental data only in the near wall region (x < 2) and are generally overestimated farther downstream in the wake region. Based on Figures 6a and 6b and above discussions it can be concluded that the current PANS modeling strategy accurately predicts the mean flow properties well in accordance with the experimental and LES results. This shows the capability of the current PANS strategy to predict accurate results for the present flow configuration at a low computational cost.

To observe further dynamic features of the flow field iso-surface of the Q-criterion is plotted, as it represents the Kelvin-Helmholtz (*K-H*) instabilities. From Figure 7 it is clear that the PANS SST *k-ω* model is able to capture these *K-H* instabilities originating from the leading edge of the square cylinder, but it fails to exhibit a fully 3D turbulent wake in the downstream, as these instabilities are damped and the large flow structures become two-dimensional. A similar trend can also be observed with the calculated dynamic viscosity ratio. As can be seen from Figure 8, in accordance with the

above-mentioned Q-criterion iso-surface, the vortex shedding is very regular and the spatial stretching of these vortices leads to large coherent quasi 2D vortices. The reason for the damping of 3D turbulent wake can be attributed to large grid size used for the simulations.

Similarly results are also compared with the experimental data in the base region (x = 1) in the cross-stream direction. Figure 9(a-e) shows that a good agreement with the experimental results is achieved by the present PANS SST k-ω model for the time-averaged values of both mean and fluctuating velocities in the transverse direction. The pronounced blockage effect caused by the square cylinder is clearly visible in Figure 9a showing the mean streamwise velocity which attains a maximum value close to 130% of the free stream velocity. Further the plot of $\overline{uv}$ at x = 1 (Figure 9e) shows that the current modeling strategy captures both the peaks, in the opposite directions, one in the shear layer of the wall ($y \approx$ 0.72) and other near the center region of recirculating region ($y \approx 0.15$) as also observed by the experimental results of Lyn *et al.* (1995).

So far the time-averaged flow properties were considered and the PANS modeling provided good predictions for both mean and fluctuating flow in both the streamwise and transverse directions. The PANS method also needs to be assessed for the periodic vortex shedding motion and the energy associated with it. For this purpose, the variation of turbulent quantities, namely, 2D turbulence kinetic energy $\left(\langle k\rangle \equiv \left(\langle u^2\rangle + \langle v^2\rangle\right)/2\right)$ and the Reynolds stresses $\left(\langle -uv\rangle\right)$, along the phase angle of the vortex shedding cycle at two different streamwise locations (x = 2 and x = 6) are considered (Figure 10), where $\langle\ \rangle$ denotes the phase averaging. The values are averaged over various cycles at a particular phase to obtain the phase-averaged values of the flow properties, as already explained in Section 3.3

Figure 10a shows that both the predicted turbulent kinetic energy and velocity correlation are in phase at x = 2 for $y \geq 0.5$, in accordance with experimental observations of Lyn *et al.* (1994). Figure 10a also shows that at x = 2 and at almost all y locations, except y = 0, Reynolds stress $\left(\langle -uv\rangle\right)$ does not change sign over the complete cycle. This is because the zone considered in Figure 10a is close to the cylinder base and it is strongly influenced by the separated shear layer. The small values of $\langle k\rangle$ are correlated with the small (absolute) values of $\left(\langle -uv\rangle\right)$ which result into drawing of the free stream fluid into the base region. Near the centerline, for y = 0 and y = 0.25, an irregularity in the relationship between the phases of $\left(\langle -uv\rangle\right)$ and $\langle k\rangle$ can be observed. At x = 6, unlike at the near wall regions, the Reynolds stress $\left(\langle -uv\rangle\right)$ does change its sign during the complete cycle. The peaks of both $\left(\langle -uv\rangle\right)$ and $\langle k\rangle$ are at different phase angles for all the y stations, but this difference is too small to conclude that both the quantities are out of phase as suggested by Lyn *et al.* (1995).

4.1 Heat Transfer Characteristics

As already stated in the Introduction, only experimental results are available for the heat transfer from a square cylinder in a cross flow. Igarshi (1985) provided the correlation for global Nusselt number:

$$\overline{Nu_g} = 0.14\left(\frac{\mu_\infty}{\mu_{wall}}\right)^{0.14} \mathrm{Re}^{0.66} \tag{29}$$

This correlation is known to be an accurate representation of the average Nusselt number results for square cylinder in a cross-flow (Sparrow *et al.,* 2004). Igarshi (1985) also measured local Nusselt number profiles around the cylinder for different Reynolds number, but as Boileau *et al.* (2013) pointed out that none of these Reynolds number corresponds to the current case (Re = 22000). Therefore Boileau *et al.* (2013) scaled two Nusselt number profiles, corresponding to the closest Reynolds number (Re = 18500 and 29600), using the correlation given by Equation (29) as

$$\overline{Nu_s} = \overline{Nu_{\exp}}\left(\frac{\mu_\infty}{\mu_{wall}}\right)^{0.14}\left(\frac{\mathrm{Re}_{current}}{\mathrm{Re}_{\exp}}\right)^{0.66} \tag{30}$$

and the local Nusselt number profile around the cylinder is calculated at Re = 22000.

Based on the effectiveness of the current modeling strategy for the flow dynamics shown in the preceding section, its capacity to predict convective heat transfer is also evaluated here. Table 3 shows the values of the global Nusselt number $\overline{Nu_g}$ obtained by the space averaging the local Nusselt number profile around the square cylinder. It is observed that the current PANS model is more close to the experimental result than the LES with wall functions used by Boileau *et al.* (2013).

A more detailed comparison of the time-averaged local Nusselt number distribution around the square cylinder with experiment data is shown in Figure 11. LES results of both the strategies (wall resolved and standard wall functions, termed as LES-WR and LES-WF, respectively) used by Boileau *et al.* (2013) are also considered to show the effectiveness of the current modeling strategy. From Figure 11 it can be observed that LES-WR of Boileau *et al.* (2013) provides better results as compared to its LES-WF and the present PANS method. As already discussed in Section 2, the near wall treatment for the energy equation is done in the present study by using the formulation given by Kader (1981) which is also applicable in the viscous shear layer.

It can be observed from Figure 11 that the time-

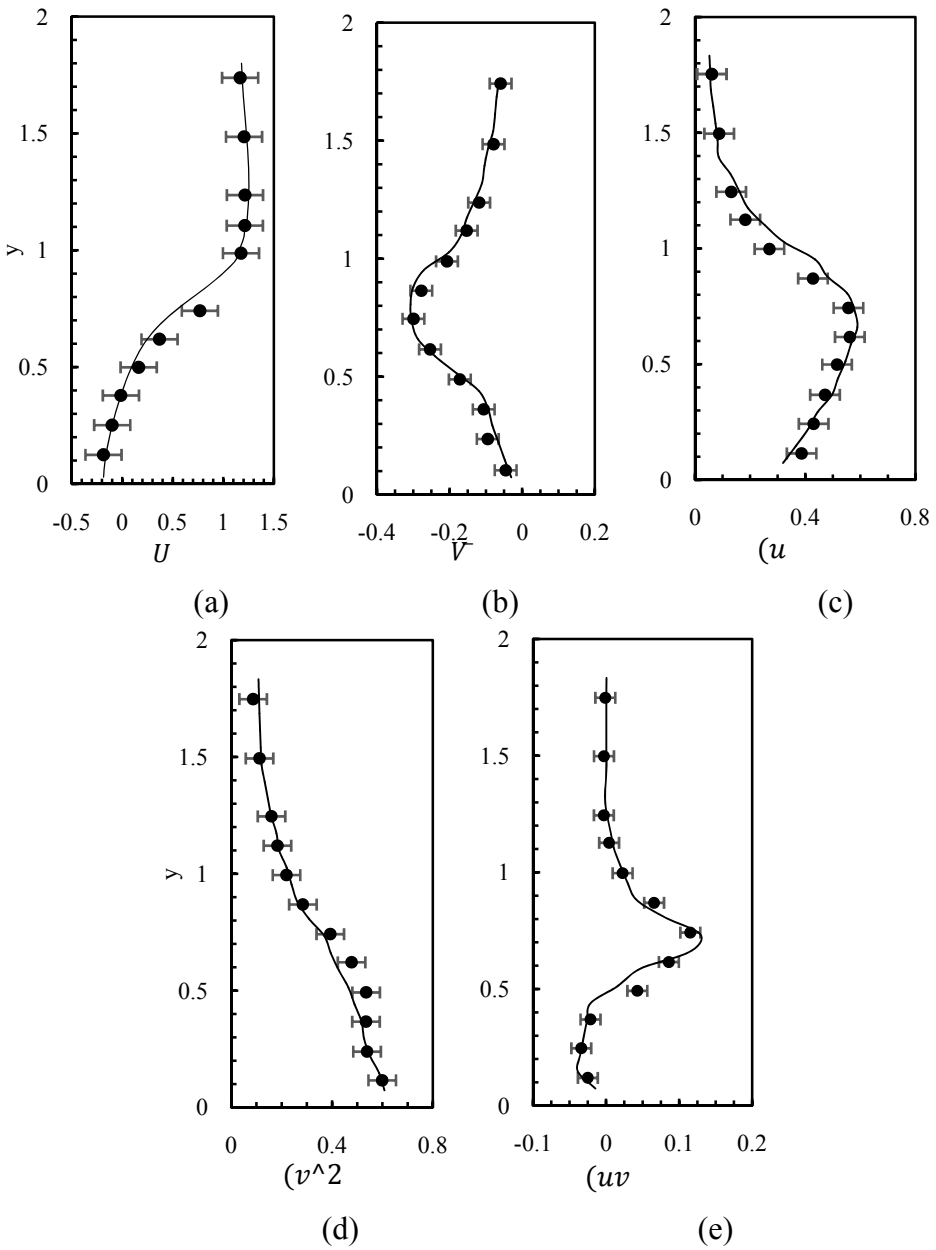

Fig. 9. Comparison of transverse profile (*x = 1*) of time –averaged streamwise and transverse velocity, streamwise and transverse velocity fluctuations and velocity correlations respectively. (● Lyn *et al.* (1995) experimental, ——— Present PANS).

averaged Nusselt number $\overline{Nu}$ is well predicted on the front side, apart from the front corner, where it underpredicts the peak values. At the rear and side faces also $\overline{Nu}$ is underestimated, probably because of the low velocity and smaller recirculation region predicted by the PANS model. Thus it can be concluded from Figure 11 that any type of wall function will fail to accurately predict the heat transfer in the region very close to the wall. This is due to the fact that any wall function is valid for either the flow with constant pressure gradient or for attached shear flows only. None of these conditions are satisfied in the case of square cylinder which involves separation at the top and bottom faces.

Even though the wall function approach associated with PANS model is not able to predict the thermal behavior quantitatively, it can still be used to get an idea of the unsteady heat transfer mechanism from the square cylinder in the cross flow. The unsteady characteristics are studied by phase-averaging the Nusselt number profile and then superimposing it with streamlines (Figure 12).

Figure 13 shows the phase-averaged quantities for different phases of the periodic flow. The *Nu* is higher at the front face than that at the top and bottom faces, because of the regular sweeping of near wall flow by the incoming cold flow, irrespective of the phase. At the rear face, due to continuous oscillation, the cold fluid is entrapped from the outer shear layer, thus the Nusselt number

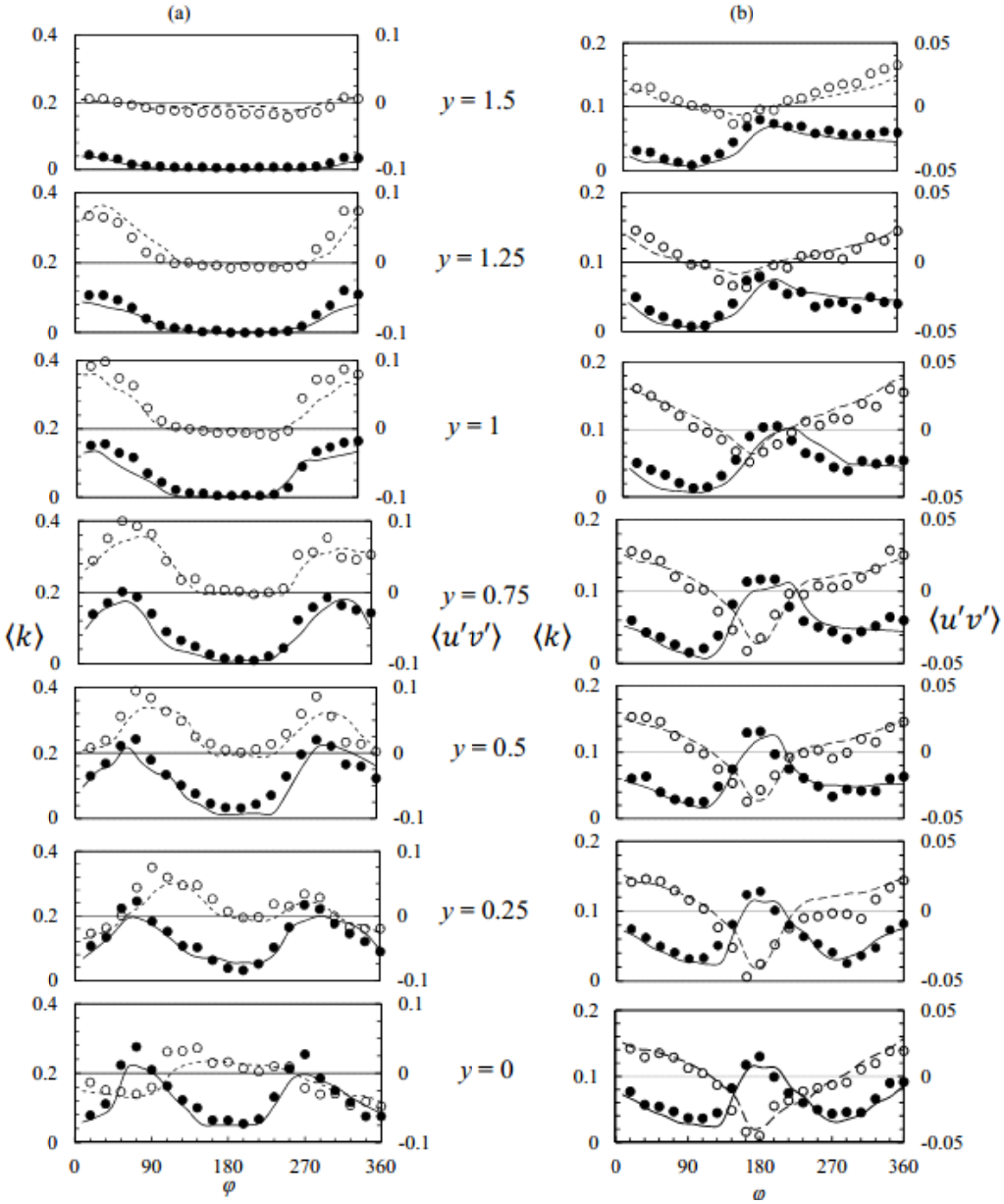

Fig. 10. Variation of $\langle k \rangle$ (● experimental, ——— computational), $\langle u'v' \rangle$ (○ Experimental, – – – computational), at two different streamwise directions, (a) $x = 2$ and (b) $x = 6$.

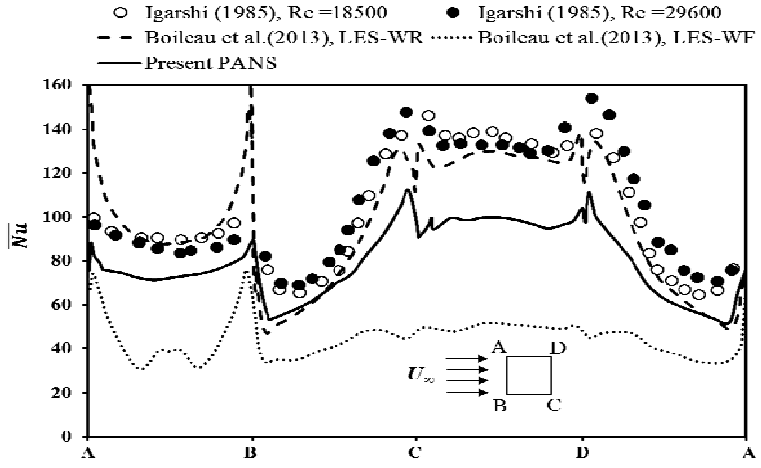

Fig. 11. Time-averaged local Nusselt number around the cylinder.

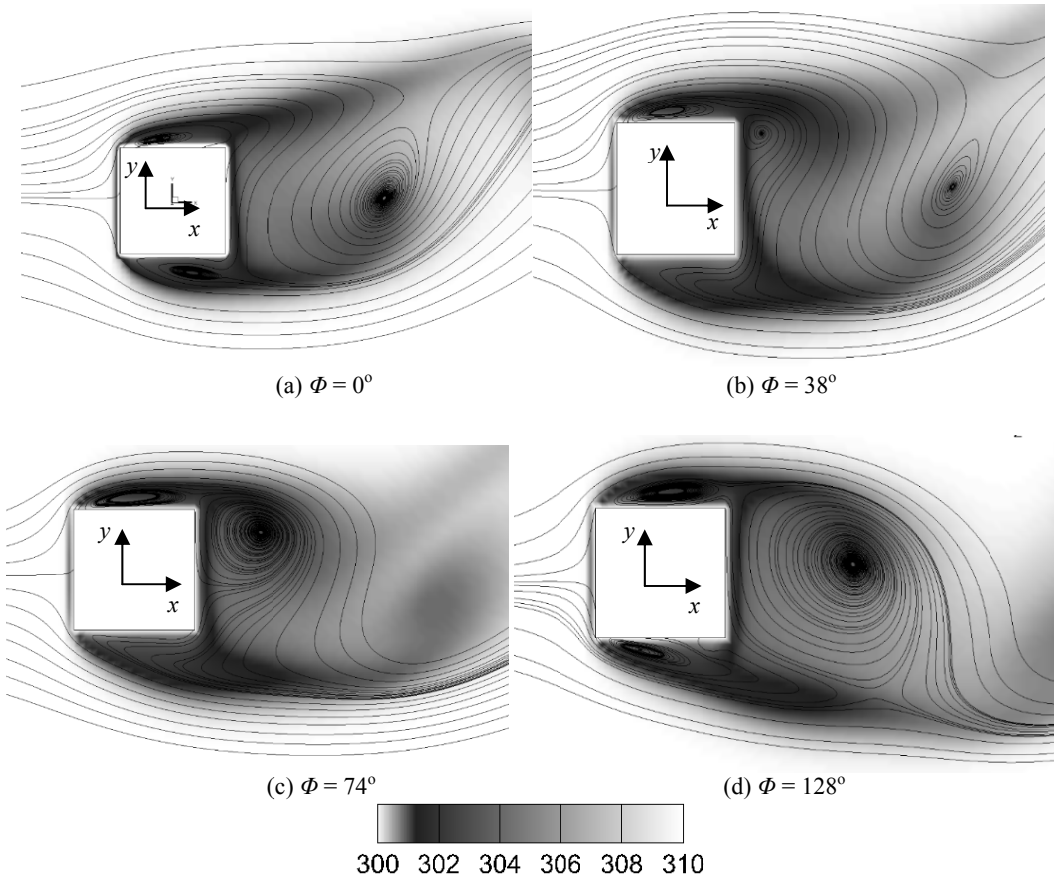

Fig. 12. Phase averaged quantities at different phase angles, Nusselt number distribution and velocity stream lines (flow is from left to right).

Table 3 Time-averaged Global Nusselt number

Case	$\overline{Nu_g}$	Error (%)
Igarshi [11], Experimental	103	NA
Boileau *et al.* (2013), LES-WF	46.1	-55
Boileau *et al.* (2013), LES-WR	101.6	-1.36
Present, PANS	82.4	-20

is higher than that at the front face and it shows a small variation with the phase. Apart from it, the flow is highly turbulent at the rear face, which further increases the Nusselt number. In the case of top and bottom faces, the variations of Nusselt number are out of phase, which is because of the transient flow of the shear layer. The value of the Nusselt number at these faces are smaller compared to those at both front and rear faces as during most of the phases the flow is entrapped in the recirculating shear regions on the faces. These recirculating regions do not interact much with the outer layer for most of the flow cycle.

Figure 14 shows the contours of the time-averaged turbulent heat flux, which can be another way to study the heat transfer. From Figure 14 it is clear that the value of the heat flux on both top and bottom faces in both directions is low due to which the heat transfer from these surfaces is small as compared to that at the rear face, which is also shown in Figures 10 and 11. At the rear corners of cylinder, strong heat flux $\left(\overline{vt'}\right)$ value is observed due to which fresh fluid is induced towards the core region of the rear face which as a result increases the heat transfer. This observation also supports the discussions made above based on the streamlines.

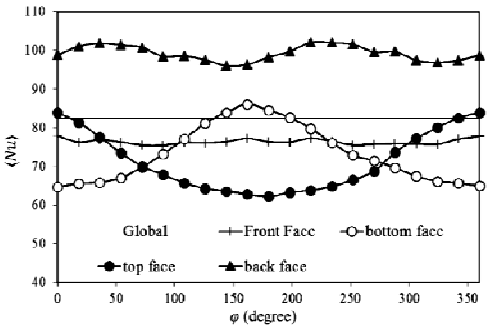

Fig. 13. Space-averaged, phase-averaged Nusselt number at different faces of cylinder.

Thus, the present study shows that the wall function used for temperature equation provide a fair idea of the unsteady heat transfer but fail to quantify it compared to the experimental observations. This is because of the complexity involved in the flow physics, which is not considered in the wall function approach.

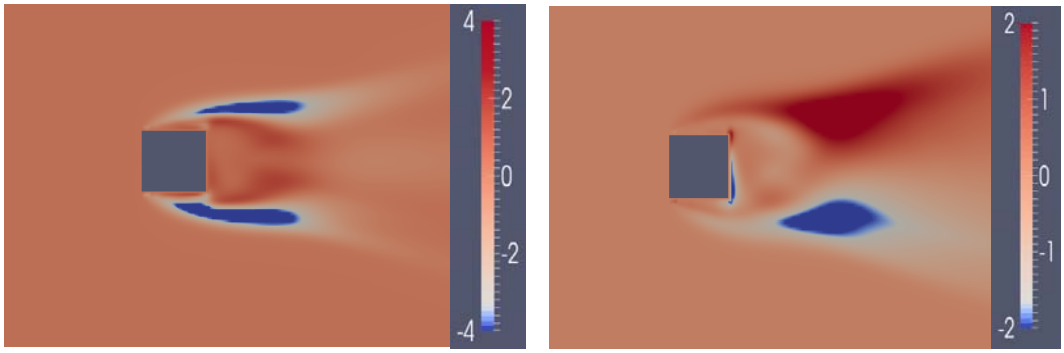

(a) (b)

Fig. 14. Contours of turbulent heat flux at center plane, (a) $\left(\overline{ut}'\right)$ and (b) $\left(\overline{vt}'\right)$.

5 CONCLUSIONS

An unsteady computational analysis of flow and heat transfer around a square cylinder at Re = 22000 is carried out using a variable resolution model strategy, PANS. The PANS SST *k-ω* model is derived and implemented in an open source code Open FOAM to carry out the simulations. The flow dynamics and heat transfer results have been compared with the experimental data reported in the literature. The heat transfer results are also compared with LES predictions reported in the literature. The computational results predicted by the present model concerning flow properties are well in accordance with the experimental data. To simulate thermal behavior, energy equation is solved with the PANS SST *k-ω* model. For the near wall treatment of the heat flux, a wall function is used which is valid for all values of y^+. The results show that the wall function approach is not able to accurately predict the time-averaged value of Nusselt number. But because of accurate predictions of flow dynamics, the blend of wall function for heat flux and PANS SST *k-ω* model, is able to predict the main features associated with the unsteady heat transfer. Therefore it can be concluded that the present PANS approach is very promising for flow dynamic predictions associated with complex industrial flows, as it is less expensive in terms of computational power. However for the prediction of heat transfer in such complex situation there is need for an improved scalar modeling and blend it with PANS method to obtain more accurate predictions.

REFERENCES

Ahmed, G. R. and M. M. Yovanovich (1997). Experimental study of forced convection from isothermal circular and square cylinders and toroids. *J. Heat Transfer.* 119:70–79.

Barone, M. F. and C. J. Roy (2006). Evaluation of detached eddy simulation for turbulent wake applications. *AIAA Journal* 44(12),3062-3071.

Basara, B., S. Krajnovic, S. S. Girimaji and Z. Pavlovic (2011). Near-wall formulation of the Partially Averaged Navier Stokes turbulence model. *AIAA Journal* 49(12),2627-2636.

Boileau, M, F. Duchaine, J. C. Jouhaud and Y. Sommerer (2013). Large-eddy simulation of heat transfer around a square cylinder using unstructured grids. *AIAA journal 51*(2), 372-385.

Durão, D., M. Heitor and J. Pereira (1988). Measurements of Turbulent and Periodic Flows around a Square Cross-Section Cylinder. *Experiments in Fluids* 6(5),298–304.

Germano, M. (1992). Turbulence: the filtering approach. *J. Fluid Mech* 238:325-336.

Girimaji, S. S. (2006). Partially-Averaged Navier-Stokes Model for Turbulence: A Reynolds-Averaged Navier-Stokes to Direct Numerical Simulation Bridging Method. *J. Appl. Mech* 73, 413-421.

Girimaji, S. S. and A. S. Khaled (2005). Partially-Averaged Navier Stokes Model for Turbulence: Implementation and Validation. *AIAA Meeting and Exhibit*.

Girimaji, S. S. and S. Wallin (2013). Closure modeling in bridging regions of variable-resolution (VR) turbulence computations. *J. Turbulence* 14(1),72-98.

Girimaji, S. S., E. Jeong and R. Srinivasan (2006). Partially Averaged Navier-Stokes Method for Turbulence: Fixed Point Analysis and comparison with Unsteady Reynolds Averaged Navier-Stokes. *J. Appl. Mech.* 73, 422-429.

Igarashi, T. (1985). Heat Transfer from a Square Prism to an Air Stream," *Int. J. Heat Mass Transfer* 28(1),175–181.

Jasak, H. (1996). Error analysis and estimation for the finite volume method with applications to fluid flows. Ph.D. Thesis, Imperial College of Science, Technology and Medicine.

Jeong, E. and S. S. Girimaji (2010). Partially Averaged Navier-Stokes (PANS) Method for Turbulence Simulations—Flow Past a Square Cylinder. *J. Fluids Eng*. 132(12).

Kader, B. A. (1981). Temperature and concentration profiles in fully turbulent boundary layers. *Int. J. Heat Mass Transfer.* 24, 1541-1544.

Lakshmipathy, S. and S. S. Girimaji (2006). Partially-averaged Navier–Stokes method for turbulent flows: k-ω model implementation. *AIAA paper*, 119.

Lakshmipathy, S. and S. S. Girimaji (2007). Extension of Boussinesq turbulence constitutive relation for bridging methods. *J. Turbulence* 8(31), 1-21.

Lübcke, H., S. Schmidt, T. Rung and F. Thiele (2001). Comparison of LES and RANS in bluff-body flows. *J. Wind Eng. Ind. Aerodyn.* 89(14), 1471-1485.

Lyn, D. A. and W. Rodi (1994). The Flapping Shear Layer Formed by Flow Separation from the Forward Corner of a Square Cylinder. *J. Fluid Mech.* 267, 353–376.

Lyn, D. A., S. Einav W. Rodi and J. Park (1995). A Laser-Doppler Velocimetry Study of Ensemble-Averaged Characteristics of the Turbulent Near Wake of a Square Cylinder. *J. Fluid Mech*. 304(3), 285–319.

Menter, F. and T. Esch (2001). Elements of industrial heat transfer predictions. In *16th Brazilian Congress of Mechanical Engineering (COBEM)* (26-30).

Menter, F. R. (1993). Zonal Two Equation k-ω Turbulence Models for Aerodynamic Flows. *AIAA Paper.* 93-2906.

Menter, F. R. (1994). Two-Equation Eddy-Viscosity Turbulence Models for Engineering Applications. *AIAA Journal* 32(8),1598-1605.

Murthi, A., D. Reyes, S. S. Girimaji and B. Basara (2010). Turbulent transport modeling for PANS and other bridging closure approaches. *In Proceedings of 5th European Conference on CFD, ECCOMAS CFD*.

Sparrow, E., J. Abraham and J. Tong (2004). Archival Correlations for Average Heat Transfer Coefficients for Non-Circular and Circular Cylinders and for Spheres in Cross-Flow. *Int. J. Heat Mass Transfer* 47(24), 5285–5296.

Wiesche, S. (2007). Large-eddy simulation study of an air flow past a heated square cylinder. *Heat Mass Transfer* 43:515-525.

Yoo, S., J. Park, C. Chung and M. Chung (2003). An Experimental Study on Heat/Mass Transfer from a Rectangular Cylinder. *J. Heat Transfer.* 125(6),1163–1170.